iScience

CellPress
OPEN ACCESS

Article

Assessment of stromal SCD-induced drug resistance of PDAC using 3D-printed zPDX model chips

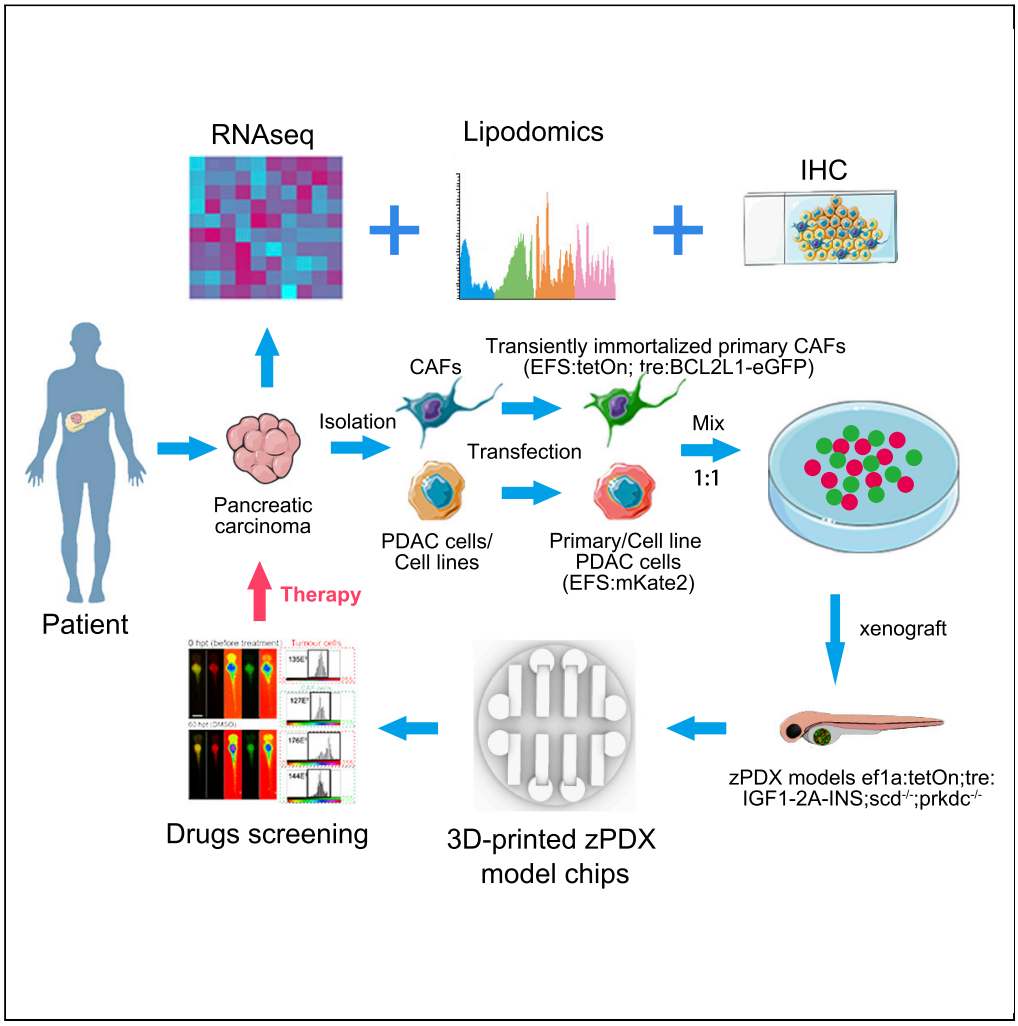

Chuntao Wu, Beiyuan Hu, Lei Wang, ..., Qiang Li, Xu Wang, Jiang Long

liq@fudan.edu.cn (Q.L.)
wangxu2013@fudan.edu.cn (X.W.)
jiang.long@shgh.cn (J.L.)

Highlights

CAFs with high SCD expression is an unfavorable prognostic factor

SCD^{high} CAFs significantly improved the drug resistance of PDAC

D-zPDX model is a promising fast-track avatars to test the responses to drugs

Wu et al., iScience 26, 105723
January 20, 2023
https://doi.org/10.1016/j.isci.2022.105723

iScience

CellPress
OPEN ACCESS

Article

Assessment of stromal SCD-induced drug resistance of PDAC using 3D-printed zPDX model chips

Chuntao Wu,[1,2,10] Beiyuan Hu,[1,2,10] Lei Wang,[3,4,10] Xia Wu,[5,10] Haitao Gu,[1,2] Hanguang Dong,[1,2] Jiuliang Yan,[1,2] Zihao Qi,[1,2] Qi Zhang,[6] Huan Chen,[7] Bo Yu,[8] Sheng Hu,[9] Yu Qian,[9] Shuang Dong,[9] Qiang Li,[6,*] Xu Wang,[3,4,*] and Jiang Long[1,2,11,*]

SUMMARY

Lipid metabolism is extensively reprogrammed in pancreatic ductal adenocarcinoma (PDAC). Stearoyl-coenzyme A desaturase (SCD) is a critical lipid regulator that was unexplored in PDAC. Here, we characterized the existence of cancer-associated fibroblasts (CAFs) with high SCD expression, and revealed them as an unfavorable prognostic factor. Therefore, primary CAFs and pancreatic cancer cells were harvested and genetically labeled. The mixture of CAFs and cancer cells were co-injected into scd$^{-/-}$; prkdc$^{-/-}$, or hIGF1/INS-expressing zebrafish to generate patient-derived xenograft models (zPDX). The models were aligned in 3D-printed chips for semi-automatic drug administration and high-throughput scanning. The results showed that chaperoning of the SCD-high CAFs significantly improved the drug resistance of pancreatic cancer cells against gemcitabine and cisplatin, while the administration of SCD inhibitors neutralized the protective effect. Our studies revealed the prognostic and therapeutic value of stromal SCD in PDAC, and proposed the application of zPDX model chips for drug testing.

INTRODUCTION

Pancreatic ductal adenocarcinoma (PDAC) is one of the most lethal malignancies with a 5-year overall survival rate (OSR) less than 10%.[1,2] The current therapeutic strategies for PDAC depend on the high-precision surgery, radiotherapy, and chemotherapy, and most patients will experience recurrence, metastasis, and drug resistance, and the prognosis is disappointing.[1,2] Given the remarkable progress of targeted and immune therapies in the past several decades, standard prescriptions for treating PDAC remain limited, and only a small proportion of patients will benefit from clinical trials of new medicine.[3] Therefore, it is crucial to identify novel druggable targets for PDAC, and meanwhile, to develop practical fast-track tools to help physicians select appropriate personalized medicines for individual patients.

The aberrances in lipid metabolism are potential therapeutic targets and typical hallmarks of multiple types of cancer, including PDAC.[4] Particularly, recent studies revealed that the desaturation of fatty acids and fatty acid chains of lipids is extensively upregulated in pancreatic cancer cells upon oncogenic insults, which may enable rapid tumor growth and flexible plasticity.[5–7] Notably, stearoyl-CoA desaturase (SCD) catalyzes the generation of monounsaturated fatty acids, oleate (C18:1), and palmitoleate (C16:1), making it the key mediator of *de novo* synthesis of unsaturated lipids.[8,9] Although SCD is not the only producer of unsaturated lipids,[10] we and other groups previously showed that tumor-expressed SCD played a significant role in promoting tumorigenesis and drug resistance in liver and lung cancers.[11–15] It was also reported that the inhibition of SCD suppressed the growth of pancreatic cancer cells *in vitro* and in the transgenic mouse model *Pdx1-Cre;LSL-Kras^{G12D} in vivo*.[16,17] However, the PDAC tumor microenvironment (TME) is characterized by an abundant extracellular matrix and dominant stromal cells, among which cancer-associated fibroblasts (CAFs) account for 90% of all cell types.[18–20] Therefore, the significance of SCD expression in non-tumor tissue and the cellular source of unsaturated lipids in PDAC TME need to be determined.

Nevertheless, the drug response of real patients with PDAC is complex and difficult to predict, and there is no effective and feasible method to determine which patients may benefit from SCD inhibitors or other regimens. At present, phenotypic analysis using patient-derived xenograft (PDX) mouse models is one of the most promising approaches to assess the potential drug responses of individual post-surgical patients, but

Continued

[1]Department of Pancreatic Surgery, Shanghai General Hospital, Shanghai Jiao Tong University School of Medicine, Shanghai 200080, China

[2]Shanghai Key Laboratory of Pancreatic Disease, Institute of Pancreatic Disease, Shanghai Jiao Tong University School of Medicine, Shanghai 200080, China

[3]Cancer Institute, Fudan University Shanghai Cancer Center, Shanghai 200032, China

[4]School of Basic Medical Sciences, Fudan University, Shanghai 200032, China

[5]Department of General Practice, Jing'an District Centre Hospital of Shanghai (Huashan Hospital Fudan University Jing'an Branch), Shanghai 200040, China

[6]Translational Medical Center for Development and Disease, Shanghai Key Laboratory of Birth Defect, Institute of Pediatrics, Children's Hospital of Fudan University, Shanghai 201102, China

[7]National Human Genetic Resources Sharing Service Platform (2005DKA21300), Fudan University Shanghai Cancer Center, Shanghai 200032, China

[8]Department of Pharmacy, Tongren Hospital, School of Medicine, Shanghai Jiao Tong University, Shanghai 200336, China

[9]Department of Thoracic Oncology, Hubei Cancer Hospital, Tongji Medical College, Huazhong University of Science and Technology, Wuhan, Hubei 430079, China

[10]These authors contributed equally

[11]Lead contact

the procedure is time-consuming and the patients with PDAC may not benefit from the outcomes in time.[21,22] In view of this, we and other groups have developed several optimized procedures to quickly generate PDX models using immunocompromised or genetically modified zebrafish (zPDX) instead of mice as hosts.[23–27] Zebrafish is highly visualized and small in size, and zPDX models can be used for fast-track *in vivo* assessment of drug responses within several days.[25,27]

In this manuscript, we reported our work on both the target identification and drug testing models. We first displayed three distinct expression patterns of SCD in human PDAC samples and revealed a significant correlation between the SCD expression level of CAFs and the OSR of patients with PDAC. To verify the different effects of SCD^{high} and SCD^{low} CAFs on tumor behaviors, especially their responses to drug administration, we designed a new protocol to generate zPDX models. On the one hand, the xenograft was a mixture of CAFs and pancreatic cancer cells, both of which were genetically modified for transient immortalization and/or fluorescent labeling. On the other hand, the zebrafish hosts bore $scd^{-/-}$; $prkdc^{-/-}$, and/or *ef1α: tetOn; tre:IGF1-2A-INS* transgenic backgrounds, in order to provide the human xenografts an immunocompromised, cytokine-humanized, and unsaturated lipid-deprived environment. The primary CAFs with different SCD expression levels were mixed with SCD^{high} PaCa2, SCD^{low} SW1990, or primary PDAC tumor cells to generate zPDX models, which were aligned in 3D-printed micro-sculptured capsule chips for drug treatment, scanning or confocal imaging, and analyses. The results showed that SCD^{high} CAFs significantly improved the survival and drug resistance of PDAC cells against gemcitabine (GEM) and cisplatin (DDP), and the personalized zPDX models served as a fast-track platform to assess the antitumor effects of novel inhibitors with or without chemotherapy.

RESULTS

Characterization of SCD expression patterns in PDAC

To assess the prognostic value of SCD expression in patients with PDAC, we first retrieved the TCGA database (version 07/20/2019). Patients with high SCD expression levels displayed a significantly worse OSR than those with low SCD expression levels, but the difference was marginal (Figure 1A, Table S1). To assess the influences of tumor-stromal ratio or immune infiltration on the association between SCD expression and OSR, we performed ESTIMATE algorithm analysis on the transcriptomic data,[28] and observed no significant correlation between the SCD expression and either stromal score or immune score (Figure 1B). We then classified the TCGA samples into four groups: $SCD^{high}Stroma^{high}$, $SCD^{high}Stroma^{low}$, $SCD^{low}Stroma^{high}$, and $SCD^{low}Stroma^{low}$ (Table S1), and a prognostic analysis of the four groups revealed that only the patients with $SCD^{low}Stroma^{low}$ displayed the best survival rate (Figure 1C). However, the ESTIMATE algorithm is an RNA-seq-based bioinformatic tool that does not provide spatial information about the SCD expression. To further investigate the spatial expression patterns of SCD, we went through the local tissue bank and manually selected 31 stroma-enriched PDAC samples that were surgically resected during 2010–2014 from the archived tissue bank of Fudan University Huashan Hospital for sectioning and staining-based analyses; the stroma-enriched samples were determined by the percentage (>60%) of the areas labeled by Masson staining and Sirius red staining, which referred to the fibrous stromal tissue (Table S2). In consistent with the TCGA data, the Kaplan-Meier curve showed that the presence of SCD^{high} stroma led to a significantly worse OSR than SCD^{low} stroma (Figure 1D). The serial sections were also stained by Alcian blue, hematoxylin, as well as antibodies of SCD and activated β-catenin (ABC), to help identify cancerous and stromal areas (Figure 1E).

Based on the expression of SCD in cancerous and stromal areas of PDAC, there existed three patterns: type I) SCD expression is low-to-moderate in cancerous area and absent in stromal area ($Tumor^{low}$ & $Stroma^{low}$); type II) SCD expression is high in cancerous area and absent in stromal area ($Tumor^{high}$ & $Stroma^{low}$); type III) SCD expression is high in both cancerous area and stromal area ($Tumor^{high}$ & $Stroma^{high}$) (Figure 1E). In stroma-enriched PDAC, the SCD^{high} stromal cell may be the significant source of the unsaturated lipids in the entire microenvironment.

Harvest of primary PDAC tumor cells and CAFs for zPDX models

To investigate the functional role of SCD^{high} and SCD^{low} stromal cells in PDAC development and drug response, we generated patient-derived xenograft models using zebrafish larvae as the hosts (zPDX models). We first obtained twelve stroma-enriched surgical-resected PDAC tissues from Shanghai General Hospital (Figure 2A, Table S3), and performed combinatorial digestion and short-term culture to isolate the tumor cells and fibroblasts separately. We successfully harvested fibroblasts (CAFs) from nine out of the

*Correspondence:
liq@fudan.edu.cn (Q.L.),
wangxu2013@fudan.edu.cn (X.W.),
jiang.long@shgh.cn (J.L.)

https://doi.org/10.1016/j.isci.2022.105723

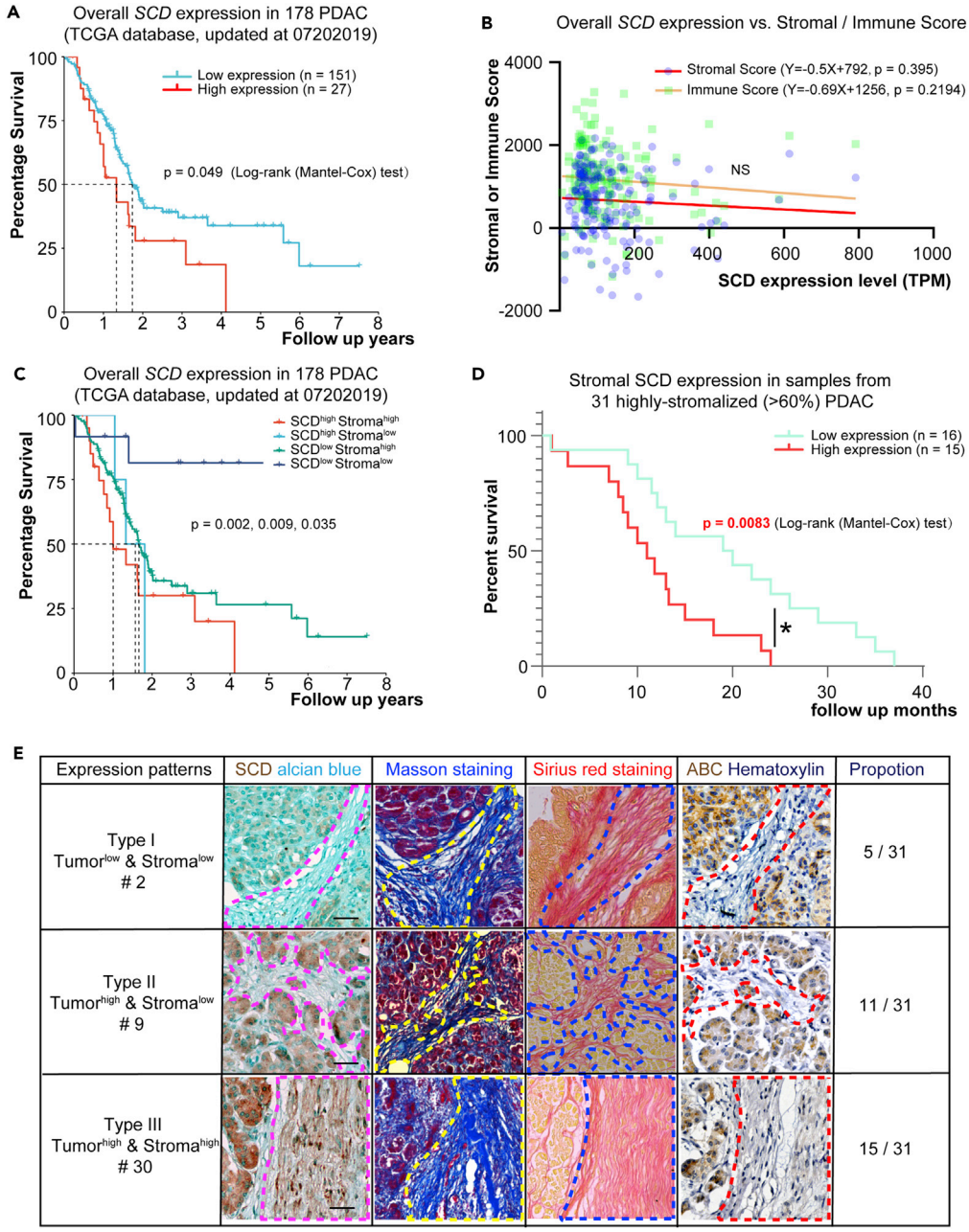

Figure 1. Expression patterns and prognosis value of SCD in PDAC samples

(A) Kaplan-Meier curves for OS in TCGA cohort (N = 176) with PDAC based on SCD expression levels.

(B) Correlation between the SCD expression levels and Stromal/Immune Scores (ESTIMATE).

(C) Kaplan-Meier curves for OS in TCGA cohort with PDAC based on SCD expression and stromal score (ESTIMATE).

(D) Kaplan-Meier curves for OS in 31 patients with stroma-enriched PDAC based on SCD expression levels. The differences between the two curves were determined by the log rank (Mantel) test.

(E) Phenotyping of the stroma-enriched PDAC samples, based on the staining of series sections, which were, from left to right, Alcian blue, SCD antibody, Masson staining, Sirius red staining, activated β-catenin antibody, and Hematoxylin. Scale bar: 20 μm. $p < 0.05$ was considered significant.

twelve samples (No. 2, 4, 5–8, and 10–12), and tumor cells from four out of the twelve samples (No. 2, 5, 7, and 8) (Table S3). All primary CAFs were transfected by our previously reported lentivirus (*EFS:tetOn; tre:BCL2L1-P2A-eGFP*),[25] which introduced green fluorescence proteins and an anti-apoptosis gene

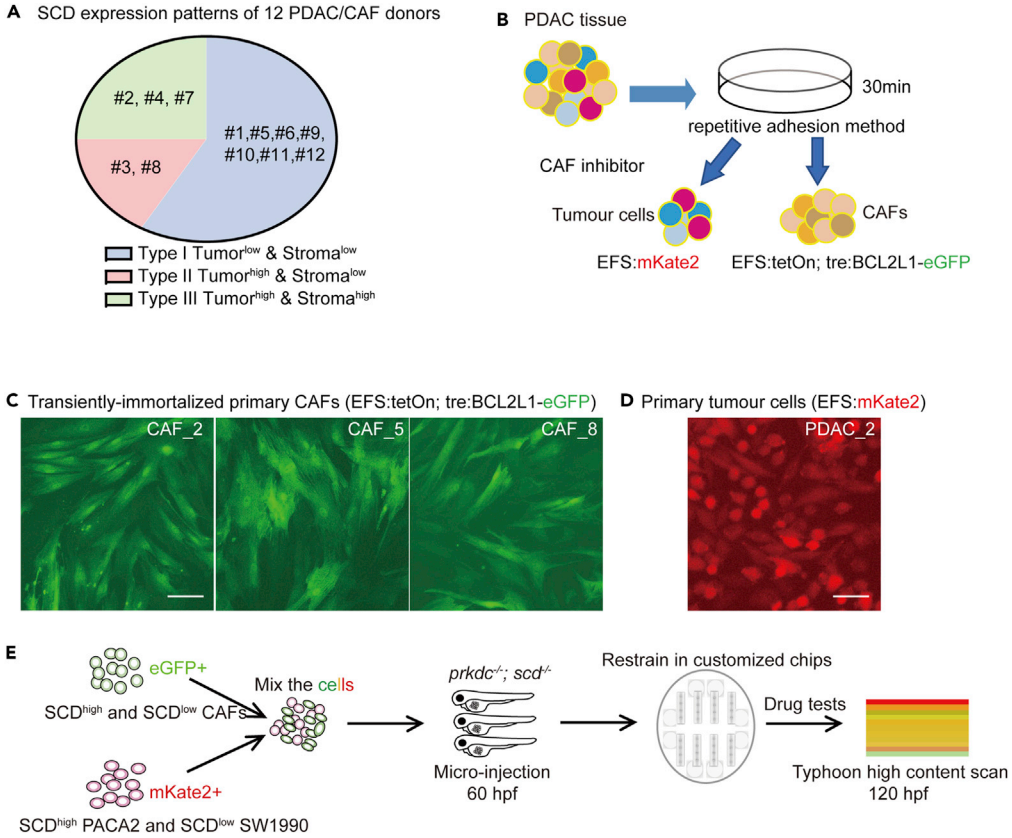

Figure 2. Harvest of primary PDAC tumor cells and CAFs for zPDX models

(A) Type proportions of the twelve stroma-enriched surgical-resected PDAC tissues from local hospital.

(B) Schematic procedure to isolate CAFs and tumor cells from primary PDAC tissues.

(C) Representative fluorescent images of the primary CAFs transfected by lentivirus (EFS: BCL2L1-P2A-eGFP).

(D) Representative fluorescent images of the primary tumor cells transfected by lentivirus (EFS: mKate2).

(E) Schematic procedure to generate the stromal-tumor-mixed zPDX models in *scd*$^{-/-}$/*prkdc*$^{-/-}$ zebrafish larvae and alignment of the zPDX models in a microarray chip. Scale bar: 20 μm.

BCL2L1 that enabled a temporary stabilization or transient immortalization of the primary cells, thus extending the observation window[25] (Figures 2B and 2C). It was still difficult to harvest and stabilize primary tumor cells from PDAC tissues. In order to compromise the low successful rate to obtain primary PDAC tumor cells, two typical pancreatic cancer cell lines, SCD^{high} PaCa-2 and SCD^{low} SW1990, were introduced. Together, the cell lines and the harvested primary tumor cells were transfected by lentivirus (*EFS: mKate2*) that introduced red fluorescence proteins (Figures 2B and 2D).

After that, the xenografts were prepared by mixing the fluorescence-labeled CAFs and PDAC cells at 1:1, followed by co-injection into the 60 hpf *scd*$^{-/-}$/*prkdc*$^{-/-}$ zebrafish larvae to generate stromal-tumor mixed xenograft models. As previously reported, the *scd*$^{-/-}$ zebrafish were generated by our group using CRISPR/Cas9 technique, which displayed developmental defects in relevant to the lack of unsaturated lipids.[12,29] Besides, *prkdc* encodes the catalytic subunit of a DNA-activated protein serine/threonine kinase, which regulates B cell differentiation, T cell receptor V(D)J recombination, and immunoglobulin heavy chain V-D-J recombination. Knockout of *prkdc* via TALENs in zebrafish led to an immune-compromised background for xenograft experiments.[30] Here, the *prkdc*$^{-/-}$ zebrafish were also generated via CRISPR/Cas9 technique; the F0 zebrafish was injected by Cas9 mRNA and sgRNA at single-cell stage, and raised into adulthood, followed by lineage identification and purification (Figure S1A). As predicted, western blot confirmed that the Prkdc protein was almost gone in homozygous *prkdc* mutants at 15dpf (Figure S1B), and the expression of *rag1*, which labels developing lymphocytes, was significantly downregulated in *prkdc*$^{-/-}$ at both 5 and 15 dpf (Figure S1C). Together, the *scd*$^{-/-}$/*prkdc*$^{-/-}$ background was

expected to provide an immunocompromised and unsaturated lipid-deprived environment for xenografts (Figure 2E). Simultaneously, a customized polydimethylsiloxane (PDMS)-based microarray chip was designed, 3D-printed, and molded to facilitate high-throughput analysis of multiple zPDX models, with the function to restrain the posture and orientation of zebrafish larvae for high-content fluorescence scanning (Figure 2E).

SCD expression determines CAF types and lipid metabolism

To characterize the primary xenografts for better grouping of zPDX models, we performed RNA-seq on all nine harvested primary CAFs (Table S4), and performed principal component analysis (PCA) to categorize the cell types. Surprisingly, the spots of the four SCD^{low} CAFs or the three SCD^{high} CAFs were naturally adjacent to each other in the PCA plot chart (Figure 3A). In addition, the correlation coefficients of the whole transcriptome among the SCD^{high} CAFs (CAF#2, CAF#4, and CAF#7), and those among the SCD^{low} CAFs (CAF#6, CAF#8, CAF#10, and CAF#11), were all above 0.95 (Figure 3B), indicating that the SCD expression levels in CAFs defined two distinct cell types: SCD^{low} CAF and the SCD^{high} CAF, which were considerably different in genetic profiles. Metabolic pathways analysis between SCD^{high} CAFs and SCD^{low} CAFs via iPath (https://pathways.embl.de) revealed that the major differences were in fatty acid metabolism (Figure S2). Further analysis on the differential expression genes (DEG) between each random pair of SCD^{low} CAF and SCD^{high} CAF showed that there were 538 DEGs shared by all comparisons (Figure 3C), including lipid metabolism genes, such as *ELOVL5*, *HACD2*, and *ASCL4*. Their expression levels were positively correlated with the *SCD* expression levels (Figure 3D).

As all samples were stroma-enriched tissues, it was rational that the SCD expression in CAFs also determined the lipid profiles of the entire PDAC microenvironment. To verify this hypothesis, we performed non-targeted lipidomics on the PDAC tissues from which the primary CAFs were harvested (Table S5). We calculated the relative frequencies of 16:1, 16:0, 18:1, and 18:1 fatty-acyl chains in all detected lipids, and obtained the unsaturation ratios (16:1/16:0 and 18:1/18:0) (Table S5). As expected, both the 16:1/16:0 and 18:1/18:0 unsaturation ratios were positively correlated with the SCD expression levels of the respective CAFs (Figures 3E and 3F).

Assembly of the zPDX microarray chips to assess different chemotherapies

After the preparation of xenografts, zebrafish hosts, and microarray chips, we assembled the model system and evaluated the protective effects of the characterized CAFs on tumor cells *in vivo*. We first mixed the nine strains of CAFs with different SCD expression with SCD^{high} PaCa-2 and SCD^{low} SW1990, to generate standardized zPDX models to specifically assess the role of stromal SCD. The models were then mounted in the customized micro-sculptured microarray chips for drug administration, high-throughput scanning, and quantitative assessment.

The bottom of the microarray chip was casted in a 9 cm plate, with eight chambers in each plate. In each chamber, there was a small liquid storage tank and a microfluidic agarose-based structure with four fish-shape restrain capsules in alignment (Figures 4A and S3). After mounting zPDX models in the capsules, we sealed the chambers with 3D-printed resin covers (Figures 4A and S3). There were two holes left on the cover, enabling us to add drugs and replace the solution every 6 h using needles and low-speed peristaltic pump (Figures 4A and S3). The molds for making PDMS chambers and agarose restrain capsules were designed in Rhino, and generated by a 3D printer using the photosensitive resin (Figure S3).

For high-throughput scanning, the zPDX models were scanned in a GE typhoon scanner at two time points, 0 hpt (hours post drug treatment) and 60 hpt. A total of six different chemotherapy regimens were tested (Gemcitabine (GEM), Tegafur (TGO), Cisplatin (DDP), Paclitaxel (PTX), Vinorelbine (NVB), and Irinotecan (CPT-11)), and the concentrations were determined as the half of the maximal tolerance dosage (MTD). The MTD was obtained from a preliminary test performed as previously reported.[12,15] In short, 60 hpf zebrafish were raised in 6-well plates (6 fish per will) in solutions containing different step concentrations of a certain drug, the solution was changed every day, and their survival conditions were recorded until 120 hpf. The concentration at which all zebrafish survived without significant malformations and abnormal behaviors was determined as the MTD. The red fluorescent signals representing tumor cells and the green fluorescent signals representing fibroblasts were captured for quantitative analyses (Figure 4B, Table S6). To assess the net effects of CAFs on tumor cells, we performed two rounds

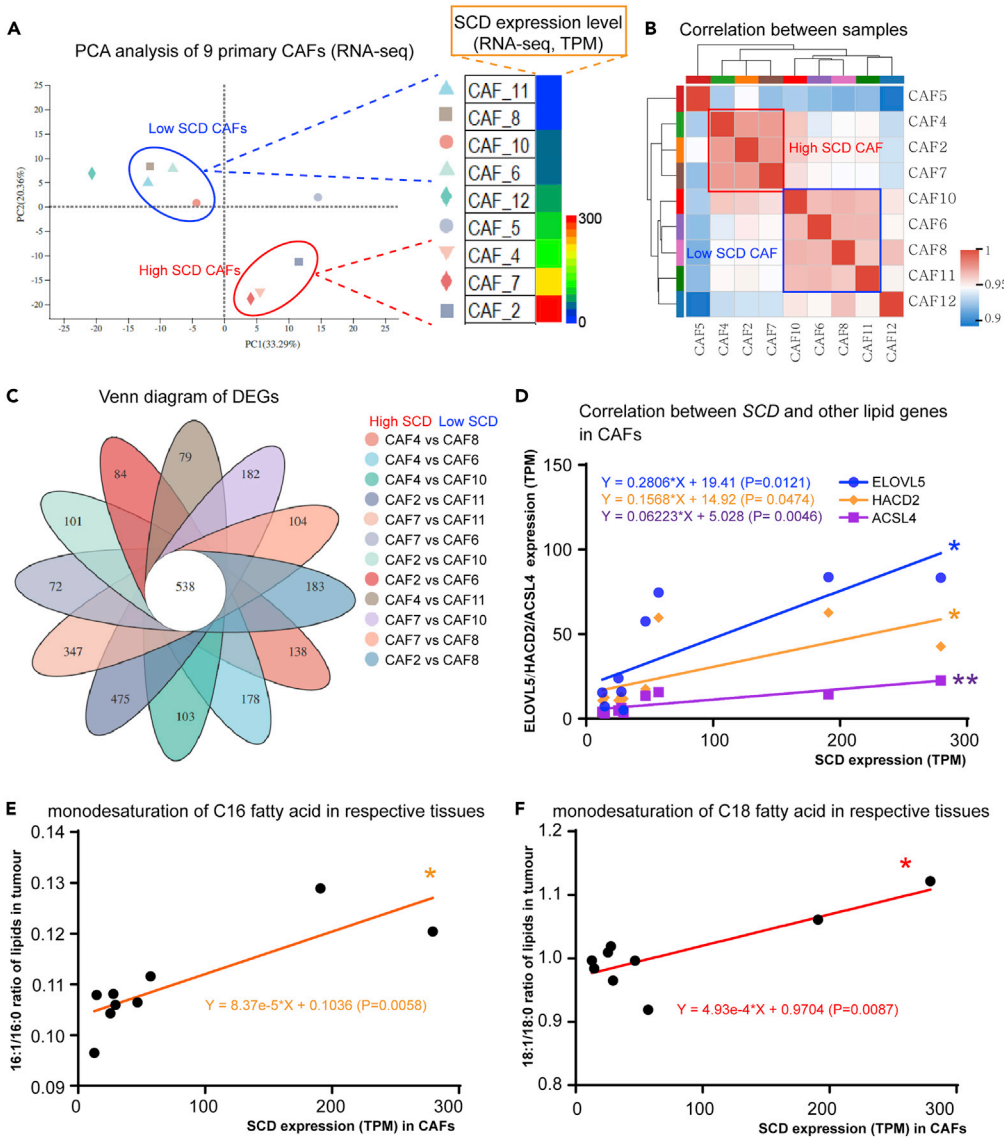

Figure 3. SCD expression characterizes CAF types and lipid metabolism

(A) PCA analysis of 9 primary CAFs depending on SCD expression level (RNA-seq).

(B) Correlation analysis of the CAFs' transcriptomic profiles.

(C) 538 DEGs identified among 12 paired primary SCD^{low} CAF and SCD^{high} CAF.

(D) Correlation analysis on SCD expression level and lipid genes (ELOVL5, HAC02, and ACSL4) on CAFs.

(E) Correlation analysis between SCD expression in CAFs and the C16 fatty acid monodesaturation ratios in the respective PDAC tissues.

(F) Correlation analysis between SCD expression in CAFs and the C18 fatty acid monodesaturation ratios in the respective PDAC tissues. $p < 0.05$ was considered significant.

of normalization, first divided the fluorescent intensity of tumor cells co-injected with CAFs by the fluorescent intensity of tumor cells injected alone, and then divided the value of the drug-treated group by the value of the DMSO-treated control group. After two rounds of normalization, the results were further logarithmically calculated and demonstrated in a heatmap for better visualization (Figure 4C). Compared with SCD^{low} CAFs, SCD^{high} CAFs significantly improved the viability of Mia-PaCa2, a SCD^{high} pancreatic cancer cell line, in the zPDX models treated by GEM, TGO, and DDP; SCD^{high} CAFs also significantly improved the viability of SW1990, a SCD^{low} pancreatic cancer cell line in zPDX models treated by GEM, DDP, and PTX (Figure 4C).

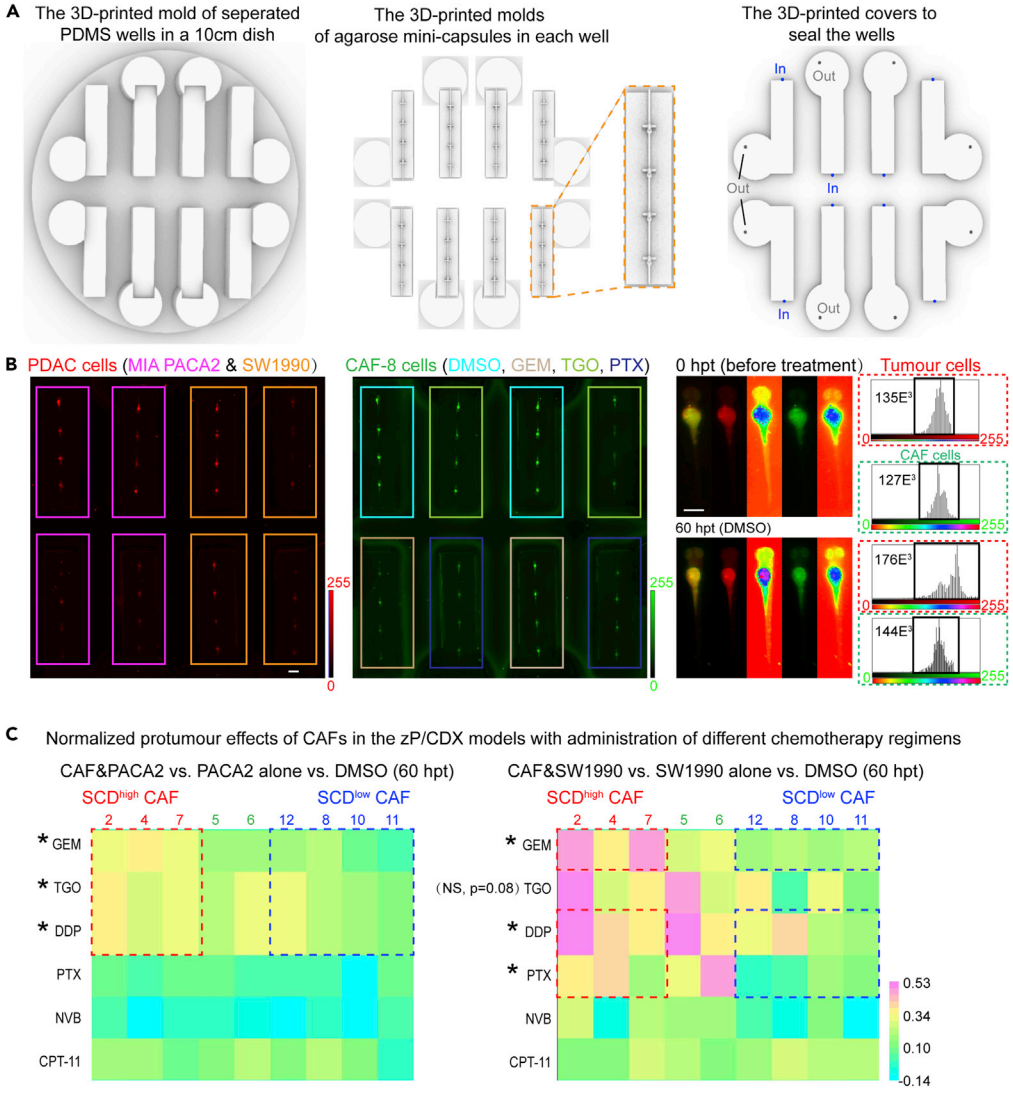

Figure 4. Assembly of the zPDX microarray chips to assess their responses to chemotherapy

(A) 3D-printed molds of separated PDMS wells, agarose mini-capsules, and the covers of the well. Two holes on each cover to add drugs and replace the solution every 6 h.

(B) The representative scanning images of a zPDX model chip at 0 hpt (hours post drug treatment) and 60 hpt in green and red fluorescent channels, and a representative quantitative analysis for the fluorescent signals of the tumor cells (red) and the fibroblasts (green).

(C) Summarized heatmap of the normalized viability of PDAC tumor cells in the drug-treated groups compared to the DMSO-treated control group. GEM: Gemcitabine; PTX: Paclitaxel; CPT-11: Irinotecan; NVB: Vinorelbine; DDP: Cisplatin; TGO: Tegafur. Scale bar: 300 μm.

SCD inhibitors alleviated the pro-tumor and drug-resistant properties of SCD^{high} CAFs

Our results suggested that SCD^{high} CAF promoted the drug resistance against GEM and DDP in PDAC, regardless of the SCD expression level in tumor cells themselves. Therefore, we employed zPDX again to test the feasibility of targeting SCD to weaken the protective effect of the SCD^{high} CAF.

To improve the stability of the zPDX and the survival of patient-derived xenografts, here, we used *ef1α:tetOn*; tre:*IGF1-2A-INS*; *scd*$^{-/-}$ instead of *prkdc*$^{-/-}$; *scd*$^{-/-}$ background. The *ef1α:tetOn;* tre:*IGF1-2A-INS* humanized transgenic cascade was generated to enable the zebrafish hosts to conditionally express two pro-growth human cell factors (Figure S4A). By design, the transgenic cascade can be induced by doxycycline (DOX) to express human IGF1 and insulin (Figure S4A). Whole-mount antibody staining for human

IGF1 confirmed the DOX-dependent expression of the transgenic cascade (Figure S4B). ELISA assays also showed that the INS and IGF1 levels in the transgenic zebrafish were dosage dependent and the normalized concentration of IGF1 and INS in whole zebrafish treated by 40 μg/mL was approximately 90 μg/L and 35 μg/L (Figure S4C). As a reference, rhIGF1 supplemented in common serum-free medium was around 1–100 μg/L.

Significantly, the comparison of the xenografted cell viability between *ef1α:tetOn*; tre:*IGF1-2A-INS* treated and not treated by DOX confirmed that the expression of the humanized transgenic cascade significantly improved the survival of human cells *in vivo*, thereby improving the stability of the zPDX models (Figures S5A and S5B). On the contrary, the comparison of the xenografted cell viability between $prkdc^{+/-}$ and $prkdc^{-/-}$ at 60–120 hpf indicated that this immunodeficient background did not significantly improve the cell survival in hosts at early stages (Figures S5A and S5B). In other words, when the zebrafish hosts have not developed fully functional lymphocyte immunity, $prkdc^{-/-}$ may not be essential for xenograft survival. So, here we integrated *ef1α:tetOn*; tre:*IGF1-2A-INS* instead of $prkdc^{-/-}$; as the genetic background for hosts.

Three different small molecule inhibitors of SCD, MK-8245 (15 μg/mL), MF-438 (2 μg/mL), and Aramchol (10 μg/mL) (Figure 5A) were employed to test their capacity to alleviate the pro-tumor properties of SCD^{high} CAFs and to improve the efficiency of chemotherapy. The working concentrations were determined as half of the maximal tolerant dosages, which is the maximal concentration of certain inhibitor allowing 60 hpf zebrafish larvae to survive for another 60 h without obvious malformations or abnormal behaviors.

The xenografts used in the combinatory drug testing were 1:1 mixtures of the primary pancreatic cancer cells from patient#2 (PDAC#2) and primary SCD^{high} CAFs from patient#2 and #7 (CAF#2 and CAF#7). We chose patient #2 because SCD was generally expressed in both cancerous tissue and stromal tissue. MET and KRAS/HRAS antibodies labeled the cancerous areas, while α-SMA (ACTA2), CXCR5, and COL6A2 antibodies labeled the stromal areas (Figure 5B). Besides, CAF#7 was selected as an alternative SCD^{high} CAFs.

The xenografts were injected into 60 hpf *ef1α:tetOn; tre*; *IGF1-2A-INS;* $scd^{-/-}$ zebrafish larvae to do the combinatory drug testing. Doxycycline was administered at 48 hpf to induce the expression of the human cytokines to nourish the human xenografts. There were nine groups including control for PDAC#2 & CAF#2 and PDAC#2 & CAF#7 zPDX models: DMSO control, GEM, GEM + aramchol, GEM + MK8245, GEM + MF438, DDP, DDP + aramchol, DDP + MK8245, and DDP + MF438. The relatively fewer samples allowed us to perform high-resolution confocal imaging of individual models and cell counting analysis. After drug administration, all three SCD inhibitors significantly improved the efficiency of GEM and DDP (Figures 5C and 5D), among which aramchol showed the best outcomes in both zPDX models (Figures 5C and 5D).

In conclusion, our studies revealed that the SCD expression by CAF and its derived unsaturated fatty acid significantly improved the resistance of PDAC cells against DDP and GEM (Figure 5E). We also showed how to genetically manipulate zebrafish to provide fast and convenient hosts for patient-derived xenografts, including immune-compromise, cytokine humanization, and metabolic environment modification (unsaturated lipid deprivation) (Figure 5F). When evaluating the combinatory regimens of routine chemotherapy and novel inhibitors of a specific target (Gene X) (We may call it "chemotherapy PLUS"), the strategy of using improved zPDX models may be employed to accelerate the decision-making of personalized drugs (Figure 5F).

DISCUSSION

zPDX models are promising avatars for personalized therapy

Precision medicine requires the personalized design of therapeutic strategies, and many *in vitro* and *in vivo* models are being proposed as avatars of patients to facilitate this process.[31] The most-studied *in vivo* avatars are xenograft models using murine as hosts, e.g. the patient-derived tumor cells are transplanted into immune-compromised mice, followed by the parallel drug efficacy assessment, with the hope to provide the best choice for patients.[22] Meanwhile, the most popular *in vitro* avatars for drug testing is the primary organoid culture, which is superior to traditional cell culture in the term of the natural structure and cellular

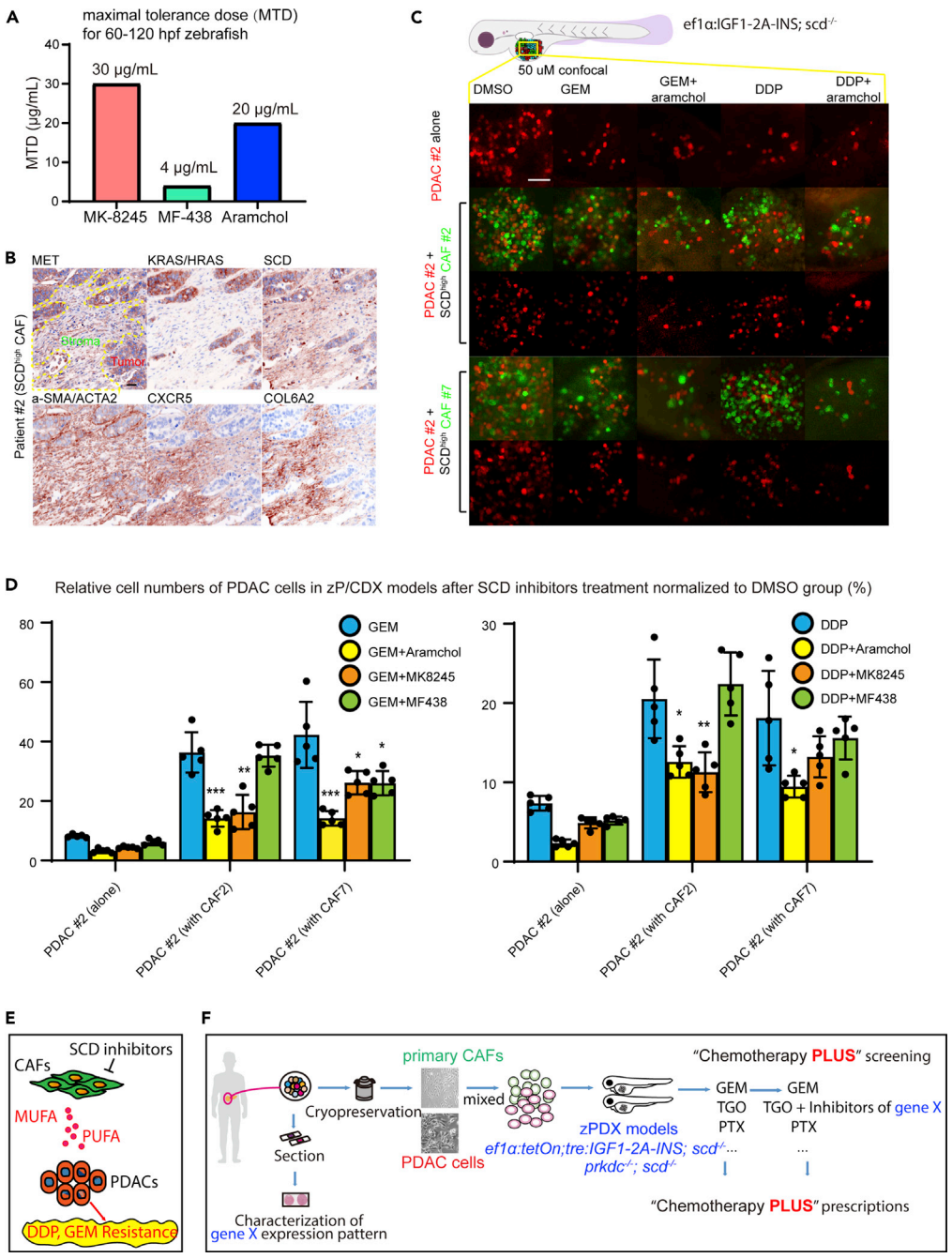

Figure 5. SCD inhibitors repress the pro-tumor and drug-resistant properties of SCD^{high} CAFs

(A) Maximal tolerance dose (MTD) of three SCD inhibitors (MK-8245, MF-438, and Aramchol) for 60 hpf zebrafish larvae.

(B) Representative images of immune staining of MET, KRAS, HRAS, ACTA2, CXCR5, and COL6A2 in the PDAC tissues from patient #2.

(C) Representative confocal fluorescent images of the lateral views of the zPDX models xenografted by PDAC #2 (Red) mixed with CAFs from patient #2 or #7 (Green) treated by GEM, DDP with or without the administration of the SCD inhibitor aramchol.

(D) Statistics of the fluorescence intensity of the PDAC cells in chemotherapy-treated zPDX models with or without all three SCD inhibitors.

(E) Schematic diagram of the CAF-derived unsaturated fatty acids contributing to the drug resistance of PDACs against DDP and GEM.

(F) Application of the "chemotherapy PLUS" protocol to fast predict the therapeutic efficacy of novel target inhibitors using zPDX models. Scale bar: 50 μm. $p < 0.05$ was considered significant.

composition, but it is still an *in vivo* system.[32] Both the mouse PDX and primary organoid are time-consuming and the success rates are low.[22] zPDX models do not need as many cells as murine PDX models required, and therefore, can be quickly generated in enormous numbers without multiple subcloning. The shorter time between the harvest of tissue and the xenografting also lowers the risks of senescence and "genetic drifting" of the primary cells. In our protocols, we introduced anti-apoptosis gene, *BCL2L1*, to the co-injected stromal cells, in order to further enhance the stability of the model system. Besides, zebrafish hosts are highly visualized, and researchers are able to trace the small changes in behaviors of tumor cells at the single-cell resolution *in vivo*, which also helps shorten the testing time.[33]

Another advantage of zebrafish host is the flexibility to perform genetic modification. In the current study, we displayed the connivance to knockout the zebrafish homologous gene of the proposed human target, SCD, to avoid the influence of the metabolic environment *in vivo*. If the same modifications were carried out on mice hosts, it would be very time-consuming. In addition, the mutation can be combined with immune-compromised background, and due to the high fertility (200–300 fertilized eggs per mate per pair), we can obtain many zebrafish hosts very soon without expansion of a colony like we did to mice hosts. We also generated transgenic zebrafish that expressed pro-growth human cell factors to further stabilize the human xenografts. The above optimizations enabled us to generate personalized PDX models for patients with PDAC with high success rates.

Strategy of mixed PDX modeling

Although PDX models directly utilize the patients' cells as xenografts, it does not mean the xenograft faithfully replicates the structures and behavior of the donor's tumor. In fact, PDAC microenvironment consists of a diversity of non-tumor tissues, particularly the CAFs.[18–20] In the current study, we performed co-xenograft of CAFs and tumor cells at a 1:1 ratio, and in the clinical application, the personalized zPDX models can be injected by the mixture at the same ratio as their biopsy shows. In the future, we may separate cancer stem cells from other cancer cells before xenotransplantation, and performed real-time imaging of the cell behaviors since the zebrafish hosts are transparent. Besides, there are multiple types of CAFs in PDAC, including secretory or inflammatory CAFs, antigen-presenting CAFs, and myofibroblastic CAFs.[34] Those CAFs were not mutually exclusive, and may coexist in the PDAC microenvironment. In the future, a better PDX model should be generated by co-injecting three or more different cell types with the same cellular composition as the primary tumor to better mimic the donor's response.

Barrier of applying zPDX for clinical purpose

The major problem of applying PDX avatars for clinical purpose is the reliability and consistency of the system. It was not rare to see how different the success rates from different groups could obtain.[22,35,36] In view of this problem, we performed micron-level 3D printing and utilized the printed mold to assembly microarray chips, which can restrain the postures of multiple zPDX models. The purpose of this procedure was to achieve semi-automatic drug administration, scanning, and data analyses in zPDX, and to minimalize the artificial errors. Our study may serve a proof-of-concept demonstration. Similarly, the harvest, isolation, and handling of the primary xenografts may also be carried out in a semi-automatic manner, as well as the injection of xenografts into the zebrafish hosts. Standardization of the entire zPDX drug testing platform needs interdisciplinary integration, and will lay the foundations for precise medicine application.

Limitations of the study

To rapidly develop PDX models and build biochips for drug screening, we choose zebrafish, which reproduce rapidly and have clearly observable morphology. However, the differences in genetic background between fish and humans may lead to unpredictable deviation of drug efficacy.

STAR★METHODS

Detailed methods are provided in the online version of this paper and include the following:

- KEY RESOURCES TABLE
- RESOURCE AVAILABILITY
  - Lead contact
  - Materials availability
  - Data and code availability

- EXPERIMENTAL MODEL AND SUBJECT DETAILS
  - Human subjects
  - Zebrafish stains and husbandry
- METHOD DETAILS
  - RNA-seq and lipidomics
  - Immunohistochemistry (IHC), Western blot, and ELISA
  - Cell line culture and lentivirus transfection
  - Isolation of primary cancer cells and fibroblasts from PDAC tissues
  - Installation of zPDX model chips
  - Chemotherapy drug administration
  - Imaging and image processing
- QUANTIFICATION AND STATISTICAL ANALYSIS

SUPPLEMENTAL INFORMATION

Supplemental information can be found online at https://doi.org/10.1016/j.isci.2022.105723.

ACKNOWLEDGMENTS

Shanghai Natural Science Foundation 14YF1400600, 18ZR1404500, and 21ZR1451600; National Natural Science Foundation of China 81402582 and 82172884; National Key Research and Development Program of China 2020YFA0803202; Key Frontier Project of Application Foundation of Wuhan Science and Technology Bureau No. 2019020701011438.

AUTHOR CONTRIBUTIONS

CT.W.: Conceptualization, data curation, writing–original draft. BY.H.: Data curation, supervision, writing–review and editing. L.W.: Data curation, formal analysis. X.W.: Data curation, formal analysis. HT.G.: Writing–review and editing. HG, Dong: Resources. JL.Y.: Writing–original draft. ZH.Q.: Investigation. Q.Z.: Resources. H.C.: Methodology. B.Y.: Investigation. S. Hu: Resources. Q.Y.: Investigation. S.D.: Investigation. Q.L.: Methodology, funding acquisition. X.W.: Conceptualization, funding acquisition, writing–review and editing. J.L.: Conceptualization, funding acquisition.

DECLARATION OF INTERESTS

The authors declare no competing financial interests.

Received: April 29, 2022
Revised: June 11, 2022
Accepted: November 30, 2022
Published: January 20, 2023

REFERENCES

1. Grossberg, A.J., Chu, L.C., Deig, C.R., Fishman, E.K., Hwang, W.L., Maitra, A., Marks, D.L., Mehta, A., Nabavizadeh, N., Simeone, D.M., et al. (2020). Multidisciplinary standards of care and recent progress in pancreatic ductal adenocarcinoma. CA. Cancer J. Clin. *70*, 375–403. https://doi.org/10.3322/caac.21626.

2. Mizrahi, J.D., Surana, R., Valle, J.W., and Shroff, R.T. (2020). Pancreatic cancer. Lancet *395*, 2008–2020. https://doi.org/10.1016/S0140-6736(20)30974-0.

3. Digiacomo, G., Volta, F., Garajova, I., Balsano, R., and Cavazzoni, A. (2021). Biological hallmarks and new therapeutic approaches for the treatment of PDAC. Life *11*, 843. https://doi.org/10.3390/life11080843.

4. Pavlova, N.N., and Thompson, C.B. (2016). The emerging hallmarks of cancer metabolism. Cell Metab. *23*, 27–47. https://doi.org/10.1016/j.cmet.2015.12.006.

5. Rozeveld, C.N., Johnson, K.M., Zhang, L., and Razidlo, G.L. (2020). KRAS controls pancreatic cancer cell lipid metabolism and invasive potential through the lipase HSL. Cancer Res. *80*, 4932–4945. https://doi.org/10.1158/0008-5472.CAN-20-1255.

6. Man, J., Pajic, M., and Joshua, A.M. (2020). Fats and mets, KRAS-driven lipid dysregulation affects metastatic potential in pancreatic cancer. Cancer Res. *80*, 4886–4887. https://doi.org/10.1158/0008-5472.CAN-20-3082.

7. Oatman, N., Dasgupta, N., Arora, P., Choi, K., Gawali, M.V., Gupta, N., Parameswaran, S., Salomone, J., Reisz, J.A., Lawler, S., et al. (2021). Mechanisms of stearoyl CoA desaturase inhibitor sensitivity and acquired resistance in cancer. Sci. Adv. *7*. eabd7459. https://doi.org/10.1126/sciadv.abd7459.

8. Kikuchi, K., and Tsukamoto, H. (2020). Stearoyl-CoA desaturase and tumorigenesis. Chem. Biol. Interact. *316*. 108917. https://doi.org/10.1016/j.cbi.2019.108917.

9. Ntambi, J.M., and Miyazaki, M. (2004). Regulation of stearoyl-CoA desaturases and role in metabolism. Prog. Lipid Res. *43*, 91–104. https://doi.org/10.1016/s0163-7827(03)00039-0.

10. Vriens, K., Christen, S., Parik, S., Broekaert, D., Yoshinaga, K., Talebi, A., Dehairs, J., Escalona-Noguero, C., Schmieder, R., Cornfield, T., et al. (2019). Evidence for an alternative fatty acid desaturation pathway increasing cancer plasticity. Nature *566*, 403–406. https://doi.org/10.1038/s41586-019-0904-1.

11. Lv, K., Fei, F., and Wang, X. (2019). A hint from zebrafish models of hepatic tumorigenesis: targeting stearoyl-CoA desaturase. Oncotarget *10*, 924–925. https://doi.org/10.18632/oncotarget.26645.

12. Yao, Y., Sun, S., Wang, J., Fei, F., Dong, Z., Ke, A.W., He, R., Wang, L., Zhang, L., Ji, M.B., et al. (2018). Canonical Wnt signaling remodels lipid metabolism in zebrafish hepatocytes following ras oncogenic insult. Cancer Res. *78*, 5548–5560. https://doi.org/10.1158/0008-5472.CAN-17-3964.

13. Liu, G., Feng, S., Jia, L., Wang, C., Fu, Y., and Luo, Y. (2018). Lung fibroblasts promote metastatic colonization through upregulation of stearoyl-CoA desaturase 1 in tumor cells. Oncogene *37*, 1519–1533. https://doi.org/10.1038/s41388-017-0062-6.

14. Ma, M.K.F., Lau, E.Y.T., Leung, D.H.W., Lo, J., Ho, N.P.Y., Cheng, L.K.W., Ma, S., Lin, C.H., Copland, J.A., Ding, J., et al. (2017). Stearoyl-CoA desaturase regulates sorafenib resistance via modulation of ER stress-induced differentiation. J. Hepatol. *67*, 979–990. https://doi.org/10.1016/j.jhep.2017.06.015.

15. Fei, F., Sun, S., Li, Q., Pei, Z., Wang, L., Zhang, R., Luo, F., Yu, M., and Wang, X. (2021). Combinatorial normalization of liver-derived cytokine pathways alleviates hepatic tumor-associated cachexia in zebrafish. Cancer Res. *81*, 873–884. https://doi.org/10.1158/0008-5472.CAN-20-2818.

16. Skrypek, K., Balog, S., Eriguchi, Y., and Asahina, K. (2021). Inhibition of stearoyl-CoA desaturase induces the unfolded protein response in pancreatic tumors and suppresses their growth. Pancreas *50*, 219–226. https://doi.org/10.1097/MPA.0000000000001737.

17. Gao, J., Zhang, Z., Liu, Y., Zhang, Z., Wang, M., Gong, A., Xia, L., Liao, X., Wang, D., and Zhu, H. (2021). Stearoyl-CoA desaturase 1 potentiates hypoxic plus nutrient-deprived pancreatic cancer cell ferroptosis resistance. Oxid. Med. Cell. Longev. *2021*. 6629804. https://doi.org/10.1155/2021/6629804.

18. Ligorio, M., Sil, S., Malagon-Lopez, J., Nieman, L.T., Misale, S., Di Pilato, M., Ebright, R.Y., Karabacak, M.N., Kulkarni, A.S., Liu, A., et al. (2019). Stromal microenvironment shapes the intratumoral architecture of pancreatic cancer. Cell *178*, 160–175.e27. https://doi.org/10.1016/j.cell.2019.05.012.

19. Hosein, A.N., Brekken, R.A., and Maitra, A. (2020). Pancreatic cancer stroma: an update on therapeutic targeting strategies. Nat. Rev. Gastroenterol. Hepatol. *17*, 487–505. https://doi.org/10.1038/s41575-020-0300-1.

20. Luo, G., Long, J., Zhang, B., Liu, C., Xu, J., Ni, Q., and Yu, X. (2012). Stroma and pancreatic ductal adenocarcinoma: an interaction loop. Biochim. Biophys. Acta *1826*, 170–178. https://doi.org/10.1016/j.bbcan.2012.04.002.

21. Roife, D., Dai, B., Kang, Y., Perez, M.V.R., Pratt, M., Li, X., and Fleming, J.B. (2016). Ex vivo testing of patient-derived xenografts mirrors the clinical outcome of patients with pancreatic ductal adenocarcinoma. Clin. Cancer Res. *22*, 6021–6030. https://doi.org/10.1158/1078-0432.CCR-15-2936.

22. Pauli, C., Hopkins, B.D., Prandi, D., Shaw, R., Fedrizzi, T., Sboner, A., Sailer, V., Augello, M., Puca, L., Rosati, R., et al. (2017). Personalized *in vitro* and *in vivo* cancer models to guide precision medicine. Cancer Discov. *7*, 462–477. https://doi.org/10.1158/2159-8290.CD-16-1154.

23. Yan, C., Brunson, D.C., Tang, Q., Do, D., Iftimia, N.A., Moore, J.C., Hayes, M.N., Welker, A.M., Garcia, E.G., Dubash, T.D., et al. (2019). Visualizing engrafted human cancer and therapy responses in immunodeficient zebrafish. Cell *177*, 1903–1914.e14. https://doi.org/10.1016/j.cell.2019.04.004.

24. Yao, Y., Wang, L., and Wang, X. (2020). Modeling of solid-tumor microenvironment in zebrafish (Danio rerio) larvae. Adv. Exp. Med. Biol. *1219*, 413–428. https://doi.org/10.1007/978-3-030-34025-4_22.

25. Wang, L., Chen, H., Fei, F., He, X., Sun, S., Lv, K., et al. (2019). Patient-derived heterogeneous xenograft model of pancreatic cancer using zebrafish larvae as hosts for comparative drug assessment. J. Vis. Exp. https://doi.org/10.3791/59507.

26. Wang, L., Long, J., Chen, H., Sun, S., Lv, K., Li, Q., and Wang, X. (2021). Manipulation of focal Wnt activity via synthetic cells in a double-humanized zebrafish model of tumorigenesis. Int. J. Cancer *148*, 2815–2824. https://doi.org/10.1002/ijc.33458.

27. Fazio, M., Ablain, J., Chuan, Y., Langenau, D.M., and Zon, L.I. (2020). Zebrafish patient avatars in cancer biology and precision cancer therapy. Nat. Rev. Cancer *20*, 263–273. https://doi.org/10.1038/s41568-020-0252-3.

28. Yoshihara, K., Shahmoradgoli, M., Martínez, E., Vegesna, R., Kim, H., Torres-Garcia, W., Treviño, V., Shen, H., Laird, P.W., Levine, D.A., et al. (2013). Inferring tumour purity and stromal and immune cell admixture from expression data. Nat. Commun. *4*, 2612. https://doi.org/10.1038/ncomms3612.

29. Zhang, Q., Sun, S., Zhang, Y., Wang, X., and Li, Q. (2022). Identification of Scd5 as a functional regulator of visceral fat deposition and distribution. iScience *25*, 103916. https://doi.org/10.1016/j.isci.2022.103916.

30. Jung, I.H., Chung, Y.Y., Jung, D.E., Kim, Y.J., Kim, D.H., Kim, K.S., and Park, S.W. (2016). Impaired lymphocytes development and xenotransplantation of gastrointestinal tumor cells in prkdc-null SCID zebrafish model. Neoplasia *18*, 468–479. https://doi.org/10.1016/j.neo.2016.06.007.

31. Millner, L.M., and Strotman, L.N. (2016). The future of precision medicine in oncology. Clin. Lab. Med. *36*, 557–573. https://doi.org/10.1016/j.cll.2016.05.003.

32. Tuveson, D., and Clevers, H. (2019). Cancer modeling meets human organoid technology. Science *364*, 952–955. https://doi.org/10.1126/science.aaw6985.

33. Fior, R., Póvoa, V., Mendes, R.V., Carvalho, T., Gomes, A., Figueiredo, N., and Ferreira, M.G. (2017). Single-cell functional and chemosensitive profiling of combinatorial colorectal therapy in zebrafish xenografts. Proc. Natl. Acad. Sci. USA *114*, E8234–E8243. https://doi.org/10.1073/pnas.1618389114.

34. Sperb, N., Tsesmelis, M., and Wirth, T. (2020). Crosstalk between tumor and stromal cells in pancreatic ductal adenocarcinoma. Int. J. Mol. Sci. *21*, 5486. https://doi.org/10.3390/ijms21155486.

35. Tentler, J.J., Tan, A.C., Weekes, C.D., Jimeno, A., Leong, S., Pitts, T.M., Arcaroli, J.J., Messersmith, W.A., and Eckhardt, S.G. (2012). Patient-derived tumour xenografts as models for oncology drug development. Nat. Rev. Clin. Oncol. *9*, 338–350. https://doi.org/10.1038/nrclinonc.2012.61.

36. Hidalgo, M., Amant, F., Biankin, A.V., Budinská, E., Byrne, A.T., Caldas, C., Clarke, R.B., de Jong, S., Jonkers, J., Mælandsmo, G.M., et al. (2014). Patient-derived xenograft models: an emerging platform for translational cancer research. Cancer Discov. *4*, 998–1013. https://doi.org/10.1158/2159-8290.CD-14-0001.

37. Yao, Y., Sun, S., Fei, F., Wang, J., Wang, Y., Zhang, R., Wu, J., Liu, L., Liu, X., Cui, Z., et al. (2017). Screening in larval zebrafish reveals tissue-specific distribution of fifteen fluorescent compounds. Dis. Model. Mech. *10*, 1155–1164. https://doi.org/10.1242/dmm.028811.

STAR★METHODS

KEY RESOURCES TABLE

REAGENT or RESOURCE	SOURCE	IDENTIFIER
Antibodies		
SCD antibody	Abcam	ab39969; RRID:AB_945374
ABC antibody	Millipore	05-665; RRID:AB_309887
MET antibody	Abcam	ab51067; RRID:AB_880695
HRAS+KRAS antibody	Abcam	ab240323; N/A
ACTA2 antibody	Abcam	ab7817; RRID:AB_262054
CXCR5 antibody	Abcam	ab39969; RRID:AB_945374
COL6A2 antibody	Abcam	ab182744; RRID:AB_2847919
Prkdc antibody	Abmart	PH8714; N/A
IGF1 antibody	Abcam	ab9572; RRID:AB_308724
IGF1 ELISA	Abcam	ab100545; N/A
Bacterial and virus strains		
Plasmid: pCas9	Addgene	Cat: 42876
Plasmid: pLenti-EFS:mKate2	This paper	N/A
Plasmid: pLenti- EFS:tetOn;tre: BCL2L1-eGFP	This paper	N/A
Plasmid: pTol2-ef1a:IGF1-2A-INS	This paper	N/A
Plasmid: pCS2FA-transposase	Chien lab, University of Utah	N/A
Plasmid: pT3-Cas9nls	China Zebrafish Resource Center	N/A
Biological samples		
Human samples	This study	N/A
Zebrafish samples	This study	N/A
Chemicals, peptides, and recombinant proteins		
DAB	Solarbio	DA1010
collagenase type IV	Gibco	17104019
hyaluronidase	Sigma	H3884
DNase I	Sigma	D5025
Gemcitabine	Selleck Chemicals	S1714
Paclitaxel	Selleck Chemicals	Paclitaxel
Irinotecan	Selleck Chemicals	S2217
Vinorelbine	Selleck Chemicals	S4269
Cisplatin	Selleck Chemicals	S1166
Deposited data		
SRA RNA-seq data	SRA database	https://www.ncbi.nlm.nih.gov/sra/PRJNA606346
Experimental models: Cell lines		
Mia-PaCa2	Cell Bank of Type Culture Collection of Chinese Academy of Sciences	SCSP-568
SW1990		TCHu201
HEK293T		SCSP-502
Experimental models: Organisms/strains		
scd$^{-/-}$/*prkdc*$^{-/-}$ zebrafish	This paper	N/A
ef1*α*:tetOn; tre:IGF1-2A-INS; scd$^{-/-}$ zebrafish	This paper	N/A

(*Continued on next page*)

Continued

REAGENT or RESOURCE	SOURCE	IDENTIFIER
Software and algorithms		
Prism statistics	GraphPad	Version 6.3.1
Excel	Microsoft	For Microsoft 2019
Photoshop	Adobe	CC 2018
Illustrator	Adobe	CC 2018
Majorbio software package	Majorbio	www.majorbio.com
ImageJ	NIH	1.8.0
Rhino3D	Robert McNee	Version 7.0

RESOURCE AVAILABILITY

Lead contact

Further information and requests for reagents and resources should be directed to and will be fulfilled by the lead contact, Jiang Long (jiang.long@shgh.cn).

Materials availability

This study did not generate new unique reagents.

Data and code availability

RNA-seq of the isolated CAFs was submitted to the SRA database with the project accession number: PRJNA606346, using the submission ID: SUB6935073 (https://www.ncbi.nlm.nih.gov/sra/PRJNA606346).

EXPERIMENTAL MODEL AND SUBJECT DETAILS

Human subjects

All fresh surgical-resected pancreatic cancer specimens (tatal:12, Male:6, female:6) were harvested from Shanghai General Hospital (2021). Ethical approval was obtained from the Shanghai General Hospital Ethics Committee, and written informed consent was obtained from each patient. The rest human data were either obtained from public databases or from the staining of the archived tissue sections (total:31, male:17, female:16) of Fudan University Huashan Hospital (2010–2014) with Ethical approval obtained from Fudan University Ethics Committee. Details of patient information are shown in Tables S2 and S3.

Zebrafish stains and husbandry

Zebrafish embryos, larvae and adult fish were raised under standard laboratory conditions at 28.5°C without xenograft, and 34°C after xenograft.[37] The zebrafish line *scd*$^{-/-}$ have been described previously.[12] The line *prkdc*$^{-/-}$ was generated via CRISPR-Cas9 injection at single-cell stage, followed by outcrossing and genotyping. The CRISPR-Cas9 target for *prkdc* was GGTAGACGTTGTCATCATCC, and the genotyping primers for the mutants were 5′-TTTGCTGCGGTTTGTGTTTG-′3 and 5′-GCCGCTCAAAACCAA ACCTA-′3. The line Tg (*ef1α:tetOn; tre:IGF1-2A-INS*) were generated via tol2-mediated transgene integration. The ages of the models were indicated in the main text (24hpf-120hpf, 2-5dpf, 15 dpf). All studies involving animal manipulations were approved by the Fudan University Shanghai Medical School Animal Care and Use Committee and followed the NIH guidelines for the care and use of animal.

METHOD DETAILS

RNA-seq and lipidomics

RNA-seq of the isolated CAFs was performed as previously described.[12] In short, total RNA was extracted from 100 mg PDAC samples using the RNeasy Plus Mini Kit (Qiagen 74,132), and cDNA libraries were constructed according to the Illumina protocol. The Oligo(dT) isolated mRNA were fragmented for cDNA synthesis. The cDNA fragments were purified, and connected with adaptors, followed by PCR amplification. After QC steps, the libraries were sequenced using Illumina HiSeq platform. After sequencing, the raw data were obtained and analyzed via Majorbio software package (www.majorbio.com), including DEG, metabolism pathway, PCA plotting. The original data of the RNA-seq was submitted to the SRA database

with the project accession number: PRJNA606346, using the submission ID: SUB6935073 (https://www.ncbi.nlm.nih.gov/sra/PRJNA606346). Non-targeted lipidomic profiling was also performed as previously described.[12] In brief, fresh PDAC samples were quickly frozen in liquid nitrogen, sonicated and homogenized in isopropanol. After centrifuging, the liquid supernatants were harvested for subsequent UPLC-MS assays on the ACQUITY UPLC I-Class and Xevo G2-S ESI-QTOF/MS systems. Chromatography was performed using ACQUITYUPLC CSH C18 Column, 130Å, 1.7 μm, 1 mm X 50 mm. Mass spectra scans were performed between 50 *m/z* and 2000 *m/z*, with 3 kV capillary tube voltage and 25 V cone voltage. Raw data were collected via MassLynx4.1 and analyzed by Profenesis QI to generate the normalized data.

Immunohistochemistry (IHC), Western blot, and ELISA

Immunohistochemistry on human sample was performed as follows: The slides were de-waxed by washing twice with xylene; each wash was 20 min. The slides were then rehydrated using a series of 5 min washing steps with 100%, 100%, 95%, 75% ethanol, and distilled water. Endogenous peroxidase activity was blocked using 3% hydrogen peroxide for 15 min. Antigen retrieval was performed by bathing in 10 mmol/L sodium citrate (pH 6.0) at 95°C for 20 min. After bathing in universal blocking serum for 60 min, the samples were incubated with SCD antibody (Abcam ab39969), mouse clone anti ABC antibody (Millipore 05-665), MET antibody (Abcam ab51067), HRAS+KRAS antibody (Abcam ab240323), ACTA2 antibody (Abcam ab7817), CXCR5 antibody (Abcam ab39969), COL6A2 (Abcam ab182744) at 4°C overnight. The sections were then incubated with a biotin-labelled secondary antibody and streptavidin-peroxidase for 30 min each, followed by development using DAB (Solarbio DA1010) and light counterstaining with Haematoxylin or Alcian blue. Then, the slides were dehydrated and sealed with cover slips. The Masson staining and Sirus red staining were performed as standard protocols. The Western blot against Prkdc was performed using a polyclonal antibody (Abmart, PH8714). The wholemount staining of IGF1 in zebrafish was performed using polyclonal antibody (Abcam, ab9572), followed by Cy3-conjugated secondary antibody. Two ELISA (Abcam ab100545, ab278123) was used to detecting IGF1 and insulin, the entire zebrafish was immersed into pre-measured water, followed by volume measurement, and the value was further normalized based on volume ratios. The average staining intensity of each sample was measured in 8-bit transformed images via ImageJ.

Cell line culture and lentivirus transfection

Mia-PaCa2, SW1990, and HEK293T cells were obtained from Cell Bank of Type Culture Collection of Chinese Academy of Sciences, Shanghai Institute of Cell Biology, Chinese Academy of Sciences between 2019 and 2020. All cell lines involved in our experiments were reauthenticated by short tandem repeat (STR) analysis every 6 months in our laboratory. Mycoplasma testing was detected through LookOut Mycoplasma PCR Detection Kit (Sigma, MP0035). The cells revived from frozen stocks were used within 10–20 passages or for no longer than 2 months as previously described.[12] MIA-PaCa2, SW1990 and HEK293T were cultured in DMEM (Gibco, 8117254) containing 10% fetal bovine serum (Gibco), 100 units of penicillin and 100 mg/mL streptomycin (Gibco 15140122). To generate the lentivirus, sequences of (*EFS: BCL2L1-P2A-eGFP*) and (*EFS: mKate2*) were synthesized and cloned into pCDH vectors. pCDH, pVSV-G, pGag/Pol, and pRev were used to transfect HEK293T cells. Virus-containing supernatant was collected 48 h after transfection, followed by filtration.[25] CAFs and PDAC cells were transfected with virus-containing medium in the presence of polybrene (8 μg/mL) (Sigma H9268), checked for fluorescence, and were enriched in growth medium containing 1.5 μg/mL puromycin (ThermoFisher A1113802).

Isolation of primary cancer cells and fibroblasts from PDAC tissues

As previously reported,[25] the specimens with the size around 0.5 cm^3 were obtained during an abdominal surgery, and immediately transferred into DMEM containing 10% fetal bovine serum (FBS), 10 μM Y-27632 (Cliniscience Y0503), 100 μg/mL primocin (invivogen ant-pm-1), 10 μg/mL putrescine dihydrochloride (sigma P5780), 10 mM nicotinamide (sigma N3376) and 1% penicillin/streptomycin (Gibco 15140122). The sample were removed the surrounding necrotic tissue, adipose tissue, and connective tissue, and rinsed the cancer tissue for 5–6 times with phosphate buffer (PBS) and cut the tissue into 1 mm^3 pieces. Then, the tissue was digested with 200 units/mL collagenase type IV (Gibco 17104019), 100 mg/L hyaluronidase (sigma H3884) and 20 mg/L DNase I (sigma D5025) for 15–20 min at 37°C. After digestion, the tumor mixture was plated into the full growth media including DMEM, 10% fetal bovine serum (FBS), 20 μg/mL insulin (sigma I9278), 100 ng/mL b-FGF (Gibco PHG0264), 10 ng/mL EGF (Gibco PHG0314), 10 μM Y-27632, 100 μg/mL primocin, 10 μg/mL putrescine dihydrochloride, 10 mM nicotinamide and 1% penicillin streptomycin. The mixtures were divided into two groups, one of which is added to the 100x inhibitor of pancreatic cancer fibroblasts (CHI Scientific) after repetitive adhesion procedure to remove the fibroblasts.

The cell groups were cultured for 1–2 weeks depending on the cell densities/purities and change the media every three days. The expected cell types in both group I & II can occupy over 98% in proportion in a typical successful experiment.

Installation of zPDX model chips

Cells labeled with different color fluorescent proteins were collected and counted at 1 × 10^6 cells/mL, and then the different cell lines were mixed in a certain ratio. The cells were re-suspended into 1640 medium containing 10% fetal bovine serum (FBS), 0.05% hyaluronic acid sodium salt (sigma H7630) and 0.05% methylcellulose (sigma M0262), and injected into the yolk sac of 60 hpf zebrafish using the microinjection equipment.

The microarray chip was created via 3D-printed molds on polydimethylsiloxane (PDMS) or low-melt agarose, the molds were designed in Rhino 5.0 and printed by a UV light curing 3D printer (CREALITY, LD-001), using UV sensitive resin (CREALITY, transparent). The zPDX models were aligned in the capsules along the tunnel in each pool and submerged under the E3 medium with or without drugs.

Chemotherapy drug administration

Four chemotherapy drugs Gemcitabine (GEM, Selleck Chemicals S1714), Paclitaxel (PTX, Selleck Chemicals S1150), Irinotecan (CPT-11, Selleck Chemicals S2217) and Vinorelbine (NVB, Selleck Chemicals S4269) were first dissolved in DMSO as 10 mM stocks; Cisplatin (DDP, Selleck Chemicals S1166) was dissolved in deionized water as 10 mM stocks and Tegafur (TGO, Ab142578) was dissolved in deionized water as 50 mg/mL; they were further diluted in E3 media to a final working concentration of 40 μM, 30 nM, 7 μM, 5 μM, 13 μM, and 25 μg/mL. The maximal lethal doses were determined based on preliminary tests. In a preliminary test for each drug, 60 hpf zebrafish were raised in 6-well plates (6 fish per will) in solutions containing different step concentrations, the solution was changed every day, and their survival conditions were recorded until 120 hpf. The concentration at which all zebrafish survived without significant malformations (curving tail, pericardium edema, and necrosis tissues) or abnormal behaviors (over- or no response to tap) was regarded as the MTD. Afterwards, Gemcitabine (40 μM) and Paclitaxel (30 nM), Irinotecan (7μM), Vinorelbine (5 μM), Cisplatin (13 μM) and Tegafur (25 μg/mL) were used on zebrafish to assess their effects on zPDX model.

Imaging and image processing

For high-throughput scanning, the microarray chips loaded by zPDX models were scanned using a GE Amersham Typhoon 86000 scanner, the raw original images were divided into fixed size squares containing tumors. The fluorescence signal value of each square was automatically measured based on the sum of total intensity of each pixel in ImageJ. There were four samples in each group, the fluorescence values of each sample and each cell type were collected and aligned in Excel. We performed two rounds of normalization, first divided the average fluorescent intensity value of tumor cells co-injected with CAFs by that of tumor cells injected alone, then divided the value of the drug-treated group by the value of the DMSO-treated control group. After two rounds of normalization, the results were further logarithmically calculated and demonstrated in a heatmap for better visualization. For the live zebrafish, the larvae were mounted in 3% methylcellulose (Sigma M0512) containing 200 mg/L tricaine (Sigma A5040) for live imaging. For the fixed zebrafish, the samples were subsequently balanced and mounted in 80% glycerol within a slide chamber before imaging. Besides, all section images, including bright-field and fluorescent channels, were taken with a fluorescent compound microscope, Olympus BX61. The images of intact zebrafish larvae or xenografts were obtained via either a fluorescent dissecting scope, Olympus DP73, or a Leica TCS SP8 confocal microscope system. The confocal images were demonstrated as single optical sections or maximum intensity Z projections as indicated, respectively. The value from confocal images was the average cell number of 5 samples per groups, and the cell counting was performed using area measurement and cell count tools in ImageJ.

QUANTIFICATION AND STATISTICAL ANALYSIS

All quantitative data were expressed as the mean ± SEM from at least three independent experiments (N is listed in each figure legend), with statistical differences being determined by one-way ANOVA. All Student's t-tests and one-way ANOVAs were performed in GraphPad Prism 6 (GraphPad Software Inc.) and $p < 0.05$ was considered significant.